

Combinatorial optimization of Al-doped ZnO films for thin-film photovoltaics

This article has been downloaded from IOPscience. Please scroll down to see the full text article.

2012 J. Phys. D: Appl. Phys. 45 335102

(<http://iopscience.iop.org/0022-3727/45/33/335102>)

View [the table of contents for this issue](#), or go to the [journal homepage](#) for more

Download details:

IP Address: 138.253.100.121

The article was downloaded on 22/01/2013 at 10:13

Please note that [terms and conditions apply](#).

Combinatorial optimization of Al-doped ZnO films for thin-film photovoltaics

R E Treharne¹, K Hutchings², D A Lamb³, S J C Irvine³, D Lane² and K Durose¹

¹ Stephenson Institute for Renewable Energy, Liverpool University, Liverpool, L69 7ZF, UK

² Department of Engineering and Applied Science, Cranfield University, Shrivenham, SN6 8LA, UK

³ Centre for Solar Energy Research (CSER), Glyndŵr University, OpTIC Glyndŵr, St. Asaph Business Park, LL17 0JD, UK

E-mail: R.Treharne@liverpool.ac.uk

Received 26 April 2012, in final form 4 July 2012

Published 6 August 2012

Online at stacks.iop.org/JPhysD/45/335102

Abstract

A rapid screening methodology for the development of transparent conducting oxides is presented. The methodology, based on a combination of spectrophotometry, ellipsometry and 4-point probe measurements, was used to map out the opto-electronic properties over a co-sputtered ZnO:Al₂O₃ film deposited from separate ceramic targets of ZnO and Al₂O₃. Clear distributions for the carrier density, n_e , and mobility, μ_e , are determined as a function of wt%. Al₂O₃ content within the film. A minimum resistivity value of $7.6 \times 10^{-4} \Omega \text{ cm}$ was achieved for a composition of 1.5 wt%. Al₂O₃.

(Some figures may appear in colour only in the online journal)

1. Introduction

In the field of thin-film photovoltaics the most commonly used transparent conducting oxide (TCO) materials are now those based on SnO₂ and ZnO, which have widely replaced In₂O₃:Sn (ITO) as contact layers in devices. For CdTe based PV, SnO₂:F (FTO) deposited via chemical vapour deposition (CVD)—a technique compatible with the large scale production of float glass—is the dominant TCO [1]. For amorphous/nanocrystalline Si [2], CIGS [3] and the newly emerging CZTS based [4] PV technologies, ZnO:Al (AZO) is favoured. Compared with ITO however, while the optical properties of FTO and AZO films are equivalent, their conductivities are generally inferior due to the lower achievable limits of carrier density n_e and mobility μ_e . The challenge therefore remains for the further optimization of these materials and the development of new TCO materials.

This work focuses on the development of a rapid screening methodology for the discovery and optimization of new TCO materials. The methodology is applied to a well known TCO material, Al doped ZnO [5–7], as a case study to prove the effectiveness of the method. The criteria for optimization of the TCO are kept within the context of thin-film PV which generally requires a sheet resistance of $R_{\square} < 10 \Omega/\square$ and a

transmittance of $T > 80\%$. The methodology involves the deposition of a TCO film with a deliberately non-uniform composition (i.e. doping) gradient. This is achieved via co-sputtering from separate ceramic targets of ZnO and Al₂O₃. A combinatorial analysis is then performed on the film via mapping spectrophotometry, from which opto-electronic information, e.g. refractive index $n(\lambda)$, absorption coefficient $\alpha(\lambda)$, direct band gap E_d , carrier concentration n_e etc, can be accurately extracted.

The extraction of such parameters is achieved by preparing a model of the complex dielectric permittivity, $\varepsilon(\omega)$, using it to generate a theoretical transmittance spectrum and iteratively adjusting the parameters of the model, which relate to the real physical behaviour of the material, until a suitable fit to the experimental data is achieved. The model consists of three distinct components according to

$$\varepsilon(\omega) = \varepsilon_1 + i\varepsilon_2 = \varepsilon_L + \varepsilon_{Dr} + \varepsilon_{IB}. \quad (1)$$

The first component, ε_L , represents a Lorentz oscillator of the form

$$\varepsilon_L = 1 - A_0 \left(\frac{1}{\omega_0^2 - \omega^2 + i\gamma_L \omega} \right), \quad (2)$$

where A_0 and ω_0 are the amplitude and resonant frequency of the oscillator respectively, and γ_L is a damping coefficient.

Values of ω_0 for dielectric materials are typically deep in the UV (i.e. $>7\text{ eV}$) and therefore, within the wavelength range of interest, the Lorentz oscillator generates a dielectric background which is relatively uniform except for some dispersion at shorter wavelengths.

The component ε_{Dr} accounts for the response of free carriers according to the classical Drude model [8] which assumes that the carriers undergo instantaneous, inelastic collisions and that they are solid particles which are de-localized from the surrounding metal–oxide lattice [9, 10]. The dispersion of the Drude component is given by

$$\varepsilon_{\text{Dr}} = 1 - \frac{\sigma_0}{\varepsilon_0} \left(\frac{1}{\gamma(\omega) + \frac{\omega^2}{\gamma(\omega)}} \right) + \frac{i\sigma_0}{\omega\varepsilon_0} \left(\frac{\gamma(\omega)}{\gamma(\omega) + \frac{\omega^2}{\gamma(\omega)}} \right), \quad (3)$$

where σ_0 is the dc conductivity defined by

$$\sigma_0 = n_e e \mu_e, \quad (4)$$

where n_e and μ_e are the free carrier density and mobility, respectively. The scattering factor $\gamma(\omega)$ arises from the combined interactions between free carriers and ionized impurities [11–13], phonons and crystal defects (e.g. grain boundaries). The frequency dependence of this scattering factor is modelled empirically according to

$$\gamma(\omega) = \gamma_0 - \frac{\gamma_0 + \gamma_\infty}{\pi} \left\{ \tan^{-1} \left(\frac{\omega - \omega_{\text{cross}}}{\omega_\delta} \right) \right\}, \quad (5)$$

where γ_0 and γ_∞ are the low and high frequency limits of the scattering factor and ω_{cross} and ω_δ correspond to the crossover frequency between the high and low scattering limits and the width of this transition respectively. Note that γ_0 corresponds to the value of the scattering factor under the application of a static (i.e. dc) electric field. It is this parameter that determines the carrier mobility μ_e according to

$$\mu_e = \frac{e}{m_e \gamma_0}, \quad (6)$$

where m_e is the effective electron mass. It is evident from equation (3) that as the carrier density is increased, the real part of the Drude permittivity decreases. The frequency at which this component is reduced to zero defines the boundary beyond which the material enters into a highly reflective ‘metallic’ like regime and is referred to as the plasma frequency, ω_p , defined approximately by

$$\omega_p \approx \sqrt{\frac{n_e e^2}{\varepsilon_0 m_e}}. \quad (7)$$

The inter-band transition component of the model for the dielectric permittivity can be further divided into two distinct components corresponding to contributions from direct and indirect transitions, i.e.

$$\varepsilon_{\text{IB}} = \varepsilon_d + \varepsilon_i. \quad (8)$$

The shape of the imaginary parts of each of these components, i.e. ε_{d2} and ε_{i2} , are derived from a consideration of the joint density of states (JDOS) of the valence and conduction bands

assuming a parabolic band approximation [14–16]. For direct transitions

$$\varepsilon_{d2} = \begin{cases} \frac{D}{\omega^2} (\hbar\omega - E_d)^{1/2} [1 - F_e] & \text{if } \hbar\omega > E_d + \Delta_{\text{BM}}, \\ \exp\left(\frac{\hbar\omega - E_d - \Delta_{\text{BM}}}{E_U}\right) & \text{if } \hbar\omega < E_d + \Delta_{\text{BM}}, \end{cases} \quad (9)$$

where D is related to the amplitude of the transition probability as derived from first order perturbation theory [17], and E_d is the intrinsic band gap of the material. For heavily doped metal–oxide systems the Fermi level, E_f is located within the conduction band and therefore transitions cannot occur to states within the conduction band that lie below E_f as they are already occupied. This results in an increase in the direct optical band gap of the system which is commonly referred to as a Burstein–Moss shift [18, 19] denoted by Δ_{BM} . The states within the conduction band are filled according to the Fermi distribution

$$F_e \approx \left[1 + \exp\left(\frac{\hbar\omega - E_d - \Delta_{\text{BM}}}{k_B T}\right) \right]^{-1} \quad (10)$$

and at energies $E > E_d + \Delta_{\text{BM}}$ the JDOS and thus ε_{d2} is augmented by the factor $(1 - F_e)$. Defining the minima of the conduction band as $E = 0$ it is possible to approximate the magnitude of the B–M shift to the Fermi level, i.e

$$\Delta_{\text{BM}} \approx E_f = \frac{\hbar^2}{2m_e} (3\pi n_e)^{2/3}. \quad (11)$$

Note that this is only approximately true for polycrystalline films where it has been shown that the grain size effects can also make a contribution to the band gap shift [20, 21]. Nonetheless, the relation provides another means of estimating the carrier density in addition to the value extracted from the plasma frequency according to the Drude model.

It is typical in heavily doped metal–oxide systems for there to be a density of states that extends below the conduction band minimum [22]. In a real system it is possible for these ‘tail’ states to be emptied by a population of compensating acceptors that arise from defects within the lattice. It is therefore possible for these tail states to take part in direct inter-band transitions and hence contribute to ε_{d2} at energies $E < E_d + \Delta_{\text{BM}}$. The distribution of tail states are modelled empirically using an exponential function according to the second expression in equation (9), where E_U represents the extent of the tail into the forbidden region.

Indirect transitions, that involve interactions with lattice phonons, have a much lower probability in oxide semiconductors than direct transitions but nonetheless may contribute to the shape of the dielectric permittivity. The magnitude of the contribution to the imaginary component ε_{i2} is derived from second order perturbation theory [17]

$$\varepsilon_{i2} = \frac{D'}{\omega^2} \left\{ \frac{(\hbar\omega + E_p - E_i)^2}{\exp(E_p/kT) - 1} + \frac{(\hbar\omega - E_p - E_i)^2}{1 - \exp(-E_p/kT)} \right\}, \quad (12)$$

where D' is the transition amplitude probability, E_i is the indirect band gap and E_p is the phonon energy. For metal–oxide systems, the contribution of indirect transitions act to

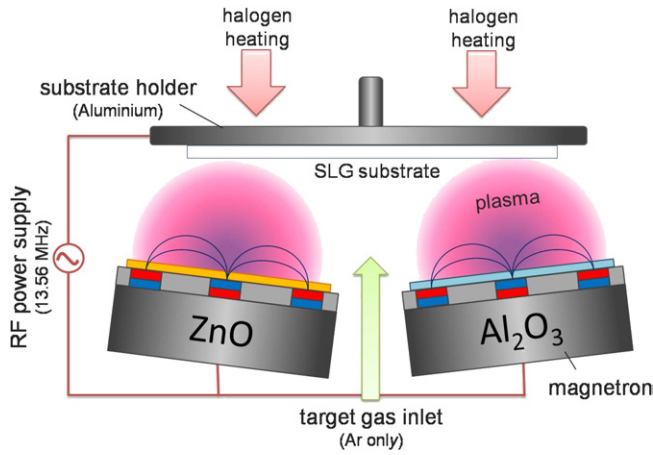


Figure 1. Schematic of co-sputtering arrangement.

broaden the cut-off in the transmittance at the direct band gap edge.

The relationship between the real and imaginary permittivity components is such that knowing one means that the other can be defined. This is according to the Kramers–Kronig relation [23, 24]

$$\varepsilon_1 = 1 + \frac{2}{\pi} \mathcal{P} \int_0^\infty \frac{\omega' \varepsilon_2(\omega')}{\omega'^2 - \omega^2} d\omega', \quad (13)$$

where \mathcal{P} denotes the principal value. The use of frequencies ω and ω' arises from the fact that a change in ε_2 at a given frequency typically induces a change in ε_1 at a second frequency.

2. Experimental details

2.1. Film deposition

Films were deposited using an AJA Orion dual chamber Phase II-J RF sputtering system. Figure 1 shows a schematic of the arrangement of magnetron guns within the chamber. The guns are positioned off centre with respect to the suspended substrate and tilted at 15° towards the substrate centre-point. The use of independent power supplies connected to each magnetron meant that they could be sputtered from simultaneously and using different RF powers. The relative growth rates from each target were calibrated via a crystal oscillator so that a ratio of 98 : 2 (ZnO (100 W) : Al_2O_3 (75 W)) was achieved at the centre of the substrate. This ratio was chosen as it is widely reported that a 2 wt% incorporation of Al_2O_3 generates films with optimum resistivities. Furthermore, a substrate temperature of 150°C and an argon pressure of 2 mTorr were chosen for the combinatorial study following preliminary investigations to determine roughly the best deposition parameters.

Films were deposited onto low Fe soda-lime glass substrates (Pilkington NSG) of size $100 \times 100 \times 3.8 \text{ mm}^3$. Substrates were cleaned using a series of DI water and isopropanol rinses followed by an *in situ* plasma etch lasting 10 min prior to deposition. Each substrate was kept stationary throughout growth so that the growth profiles from each of the ZnO and Al_2O_3 targets were deliberately non-uniform. Two

key samples were deposited: a co-sputtered ZnO/ Al_2O_3 film and a pure Al_2O_3 film. All subsequent characterization and analysis was performed on these samples.

2.2. Optical and electrical characterization

A Woollam M2000UI variable angle ellipsometer (located at Cranfield University) was used to determine the dispersion in refractive index, $n(\lambda)$, and extinction coefficient, $\kappa(\lambda)$, for the glass substrates over the range 300–1600 nm. A piece of opaque scotch tape was placed on the back surface of the glass to eliminate unwanted reflections. Spectra of Ψ and Δ , the amplitude ratio and difference in phase respectively between the s and p-polarized components of the reflected beam, were recorded at angles of 50° , 60° and 70° . A simple Cauchy model was used to extract the optical dispersion using the accompanying CompleteEASE™ software [25–27]. Ellipsometry was also used to determine the thickness profiles of the co-sputtered ZnO : Al_2O_3 and pure Al_2O_3 films.

A Shimadzu Solid Spec 3700 spectrophotometer, with automated mapping capability, was used to measure the direct transmittance over the range 250–2600 nm at 1 cm intervals over a 9 cm^2 area (i.e. 81 points). Following the measurement the data was exported to the program SCOUT3.0 [28]. This program was used to model the dielectric permittivity of the film by applying a transfer matrix method [29] to the glass/film system and iteratively fitting the transmittance data. Prior to fitting, rough estimates for the parameters of each of the model components (Drude, Lorentz, Inter-band), including the film thickness were input. A downhill simplex method [30] was then used to increment the parameters until a value for the mean squared error (MSE), calculated as the standard deviation between experimental and theoretical spectra, of <0.0001 was achieved. The key parameters (e.g. d , ω_p , γ_0) were then extracted from the model. This fitting procedure was automated over the 81 scans therefore permitting each of the extracted parameters to be mapped as a function of position over the sample.

The sheet resistance of the co-sputtered film was determined directly as a function of position across the sample surface using a Jandel RM3-NR 4-point probe located at Glyndŵr University. Hall measurements were made on uniform films using custom built equipment.

3. Results and discussion

3.1. Optical model testing

Prior to its use in the combinatorial analysis of the co-sputtered film, the model for the dielectric permittivity described above was tested by applying it to the transmittance data of an AZO film deposited on glass from a single mixed composition ZnO : Al_2O_3 (2 wt%) target. Values of the sheet resistance, carrier density, mobility and resistivity extracted from the model were compared with experimental values from van der Pauw and Hall measurements. Figure 2(a) shows the transmittance spectrum for the film and the corresponding fit achieved by the model. An excellent fit is achieved by the model over the entire spectral range with an overall MSE value

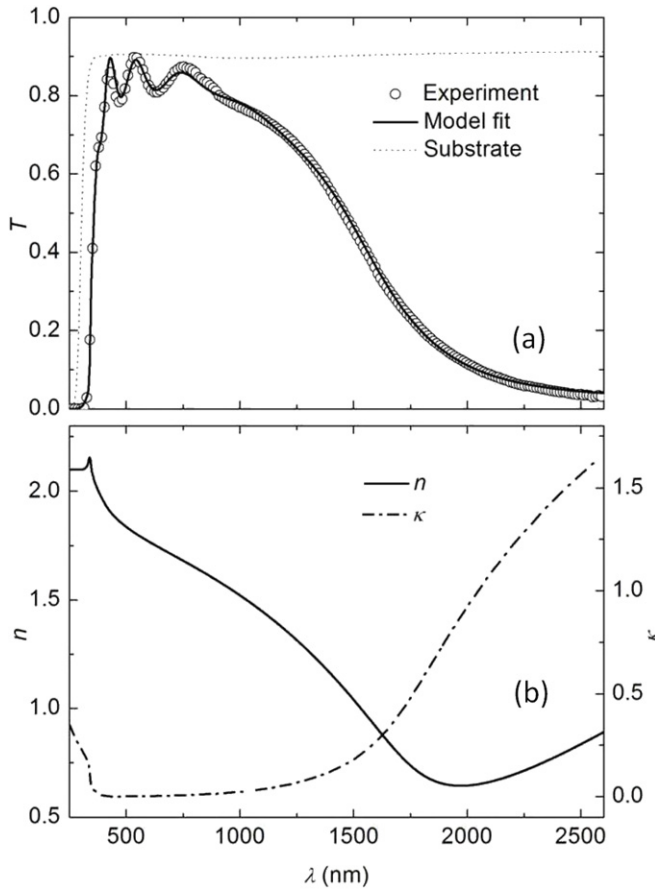


Figure 2. (a) Optical transmittance data for a ZnO:Al film, deposited from a single mixed composition (98:2 wt% ZnO:Al₂O₃) target, on glass showing the fit obtained using a model of dielectric response. (b) The subsequent dispersion relations extracted from the fit.

of 8.9×10^{-5} . The fit at wavelengths beyond the plasma frequency of the film (i.e. >1500 nm) is particularly good indicating that the extended Drude component sufficiently models the behaviour of the material's free electrons. The complete parameter set extracted from each of the separate model components is shown in table 1. The fit also provides a value for the film thickness of 452 ± 5 nm. The extracted parameter set was demonstrated to be unique by repeatedly performing the fit procedure following the significant perturbation of initial selected parameter values. The fitting always returned the same values (within the range of error) on the reduction of the MSE.

Figure 2(b) shows the corresponding n and κ dispersion extracted from the model. The features of the curves correspond directly with the expected behaviour of a degenerately doped oxide material. In the wavelength region between the direct band gap and plasma edges (350–1000 nm) it is important to note that the value for κ is very low (<0.1) indicating that the film must absorb very little in this region and that any deviation from the maximum limit of transmittance (determined by the substrate transmittance) is due to incoherent interference effects arising from reflections at the glass/film and film/air interfaces.

Table 2 shows a comparison of the film's electrical properties, as calculated from the parameters of the extended

Table 1. Parameters extracted from fitting optical transmittance of ZnO:Al film, deposit from a single mixed composition (98:2 wt% ZnO:Al₂O₃) target, using a model of dielectric response.

Model component	Parameter	Value
Lorentz oscillator	A_0 (cm ⁻¹)	3.2×10^5
	$\hbar\omega_0$ (eV)	22.3
	γ (s ⁻¹)	7.8×10^9
Extended Drude	$\hbar\omega_p$ (eV)	1.26
	γ_0 (s ⁻¹)	2.1×10^{14}
	γ_∞ (s ⁻¹)	3.0×10^{12}
	ω_{cross} (eV)	0.28
	ω_δ (s ⁻¹)	0.31
Direct transitions	E_d (eV)	3.75
	Δ_{BM} (meV)	457
	D (cm ⁻¹)	6.3×10^6
	γ_w (meV)	91
Indirect transitions	E_i (eV)	2.95
	E_p (meV)	1.7
	D' (cm ⁻¹)	0.21
	d (nm)	452
	MSE ($\times 10^{-5}$)	8.9
	\tilde{T} (300–850 nm)	0.84

Drude and inter-band model components, with those measured via van der Pauw and Hall techniques. The values of n_e and μ_e calculated from the extended Drude component are within 5% of the experimentally determined values. Values for R_\square and ρ calculated using values extracted from the model are also comparable to those determined by direct experiment. A value of $m_e = 0.31m_0$ [16, 31], determined previously for doped ZnO films, was used in the calculation of both n_e and μ_e . Note that while the inter-band component accurately models the shape of the transmittance curve in the vicinity of the direct band gap the value of n_e that it yields, calculated from the B–M shift (table 2), is larger by a factor of ~ 2 . This discrepancy is believed to be the consequence of using a simple parabolic band approximation within the inter-band transition component of the optical model. It has been shown that for degenerately doped oxides the conduction band is more commonly non-parabolic [32, 33] and a correction term is required within equation (9), according to Kane's $k \cdot p$ model [34], to account for this. Furthermore, Ruske *et al* [9] have shown that for doped ZnO films the effective mass of free carriers is not constant, as assumed within this work, but exhibits some dispersion with respect to the carrier density n_e . In future, the model should be extended to accommodate these considerations.

Nevertheless, the closeness of the model's fit to both experimental transmittance data and the consistency of the subsequent calculated electrical properties with those measured directly justifies the further use of the model in the combinatorial analysis.

3.2. Combinatorial analysis

The individual thickness profiles of the co-sputtered ZnO:Al₂O₃ (sputtered from separate pure ZnO and Al₂O₃ targets, see figure 1) and pure Al₂O₃ films deposited under the

Table 2. Comparison of experimental electrical values from a ZnO : Al film, deposited from a single mixed composition (98 : 2 wt% ZnO : Al₂O₃) target, with those obtained from optical modelling.

	R_{\square} (Ω/\square)	n_e ($\times 10^{20} \text{ cm}^{-3}$)	μ_e ($\text{cm}^2 \text{ V}^{-1} \text{ s}^{-1}$)	ρ ($\times 10^{-4} \Omega \text{ cm}$)
Experiment ^a	13.2	3.6	28.9	6.0 ^b
Ext. Drude	14.5	4.0	23.9	6.5
B–M shift	—	9.1 ^c	—	—

^a van der Pauw and Hall measurements.^b Calculated using value of $d = 451.7 \text{ nm}$ extracted from model.^c Calculated according to equation (11).

growth conditions described in section 2.1 were determined via scanning ellipsometry. Figures 3(a) and (b) show the three dimensional contour maps of the profiles. Figure 3(c) shows the subsequent profile of x wt% Al₂O₃ across the film, calculated using

$$x = \frac{\Gamma_B d_B}{\Gamma_A d_A + \Gamma_B d_B}, \quad (14)$$

where Γ and d correspond to material density and film thickness and the subscripts A and B correspond to ZnO and Al₂O₃ films, respectively. The profile shows that a useful range of composition was achieved (0–6.5%) and the composition varied almost linearly across a diagonal of the sample.

The model was applied to each of the 81 transmittance measurements made over the co-sputtered film and profiles of n_e and μ_e were calculated from the extracted parameters ω_p and γ_0 , respectively according to equations (7) and (6). The consistency with which the profiles were extracted by the model was investigated over multiple fitting attempts, each time specifying a different starting value of n_e and μ_e . In the case of n_e the profile was reproduced each time with a high degree of confidence and the resultant profile is shown in figure 4(a). However, for μ_e the profile was shown to be inconsistent for regions of the film where n_e dropped below a value of 10^{20} cm^{-3} . The value of γ_0 , from which μ_e is calculated, is only accurate if the entire plasma edge (i.e. the transition from high to low transmittance with increasing wavelength) is present within the spectra. At values $n_e < 10^{20} \text{ cm}^{-3}$ part or all of plasma edge is beyond the range of measurement and the subsequent extrapolation of γ_0 values is inaccurate. Therefore, to determine an accurate profile of μ_e it was necessary to measure the sheet resistance as a function of position using 4-point probe measurements and then calculating values of μ_e according to

$$\mu_e = \frac{1}{n_e e R_{\square} d} \quad (15)$$

and using values of n_e extracted from the optical model. The subsequent profile for μ_e is shown in figure 4(b) and the corresponding profile for ρ is shown in figure 4(c). It is clear from figure 4(c) the resistivity over the co-sputtered sample spans more than three orders of magnitude, thus demonstrating that the doping of ZnO is highly sensitive to Al₂O₃ content. A minimum resistivity of $7.6 \pm 0.3 \times 10^{-4} \Omega \text{ cm}$ was achieved for a 1.5 wt% composition of Al₂O₃ at the point $(x, y) = (4 \text{ cm}, 4 \text{ cm})$ on the sample. This point also corresponded to values of $n_e = 3.4 \pm 0.1 \times 10^{20} \text{ cm}^{-3}$, $\mu_e = 24.5 \pm$

$0.5 \text{ cm}^2 \text{ V}^{-1} \text{ s}^{-1}$, $R_{\square} = 14.4 \pm 0.2 \Omega/\square$ and $d = 528 \pm 2 \text{ nm}$. The average direct transmittance, \tilde{T} (300–850 nm), of the film across the sample remained at a level $>85\%$.

The effects of composition on the material's resultant electrical properties are shown directly in figures 5(a)–(c). A clear functional dependence of n_e on x is shown by the distribution of data points in figure 5(a). The level of n_e quickly drops as x decreases towards 0% indicating that the dominant source of carriers within the films is certainly due to the incorporation of Al rather than separate populations of native defects or impurity states. Again, it is clear that n_e is maximized at a value of $x = 1.5 \text{ wt\%}$. As x is increased further the carrier concentration drops off slowly from this maximum but remains of the order 10^{20} cm^{-3} . Figure 5(b) shows that the mobility of the free carriers is maximized at the slightly lower value of $x = 1 \text{ wt\%}$. The mobility decreases smoothly to a level $<5 \text{ cm}^2 \text{ V}^{-1} \text{ s}^{-1}$ as x increases beyond 5 wt%. This is expected as the level of impurities, e.g. Al–O phases or interstitial Al, are expected to increase the scattering of free carriers. The mobility also decreases rapidly on the other side of the maximum, as x decreases towards 0 wt%. This result is not expected as lower x values should yield a lower level of impurity scattering and hence improve mobility. The result suggests that as x decreases the level of scattering within the material, most likely due to ionized impurities arising from an excess of interstitial Zn atoms, increases and that this scattering is negated to an extent by the incorporation Al₂O₃.

The number of data points and the curves arising from them in figure 5 give confidence that the methodology generates self-consistent data. However, the graph of mobility versus composition shown in figure 5 the mobility graph shown in figure 5(b) displays some scatter beneath the upper smooth peak. These low mobility points are all associated with regions of the film that have a thickness of below 400 nm. It has been shown that grain size in polycrystalline oxide films is reduced for thinner films [35], the grain boundary density at these points is therefore higher. This results in an increase in grain boundary scattering and consequently a reduced carrier mobility. X-ray diffraction studies are required to further investigate the relationship between grain size and scattering.

4. Conclusions

The model for the dielectric permittivity of doped ZnO is used in conjunction with the SCOUT3.0 software to confidently fit transmittance data of a ZnO : Al deposited from a standard ZnO : Al₂O₃ (98 : 2 wt%) target. The fitting yields values

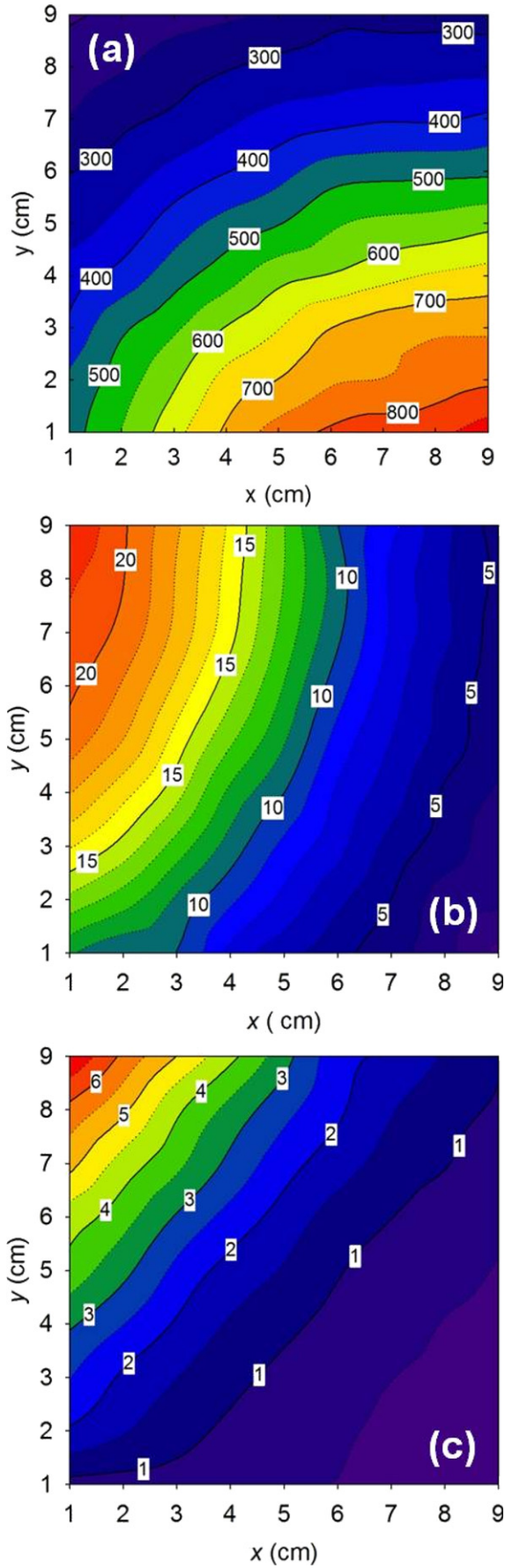


Figure 3. Profiles of (a) ZnO thickness (nm), (b) Al₂O₃ thickness (nm) and (c) wt% Al₂O₃ calculated by combining profiles (a) and (b).

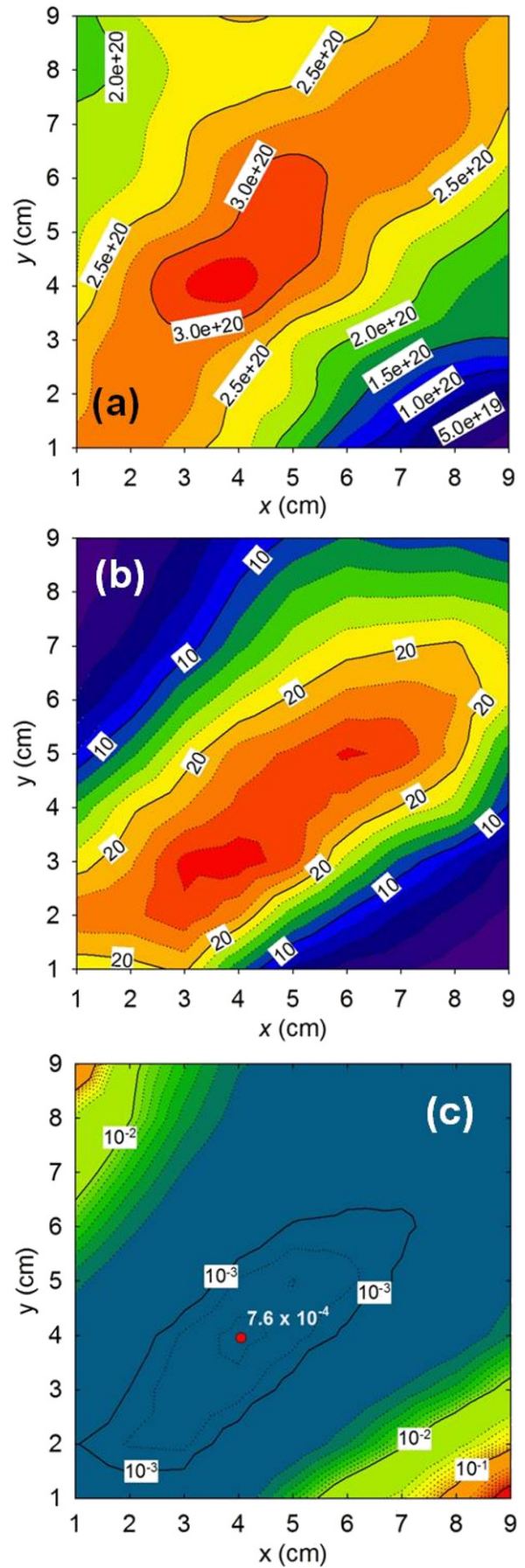


Figure 4. Profiles of (a) carrier concentration, n_e ($\times 10^{20} \text{ cm}^{-3}$), (b) carrier mobility, μ_e ($\text{cm}^2 \text{ V}^{-1} \text{ s}^{-1}$) and (c) resistivity, ρ ($\Omega \text{ cm}$).

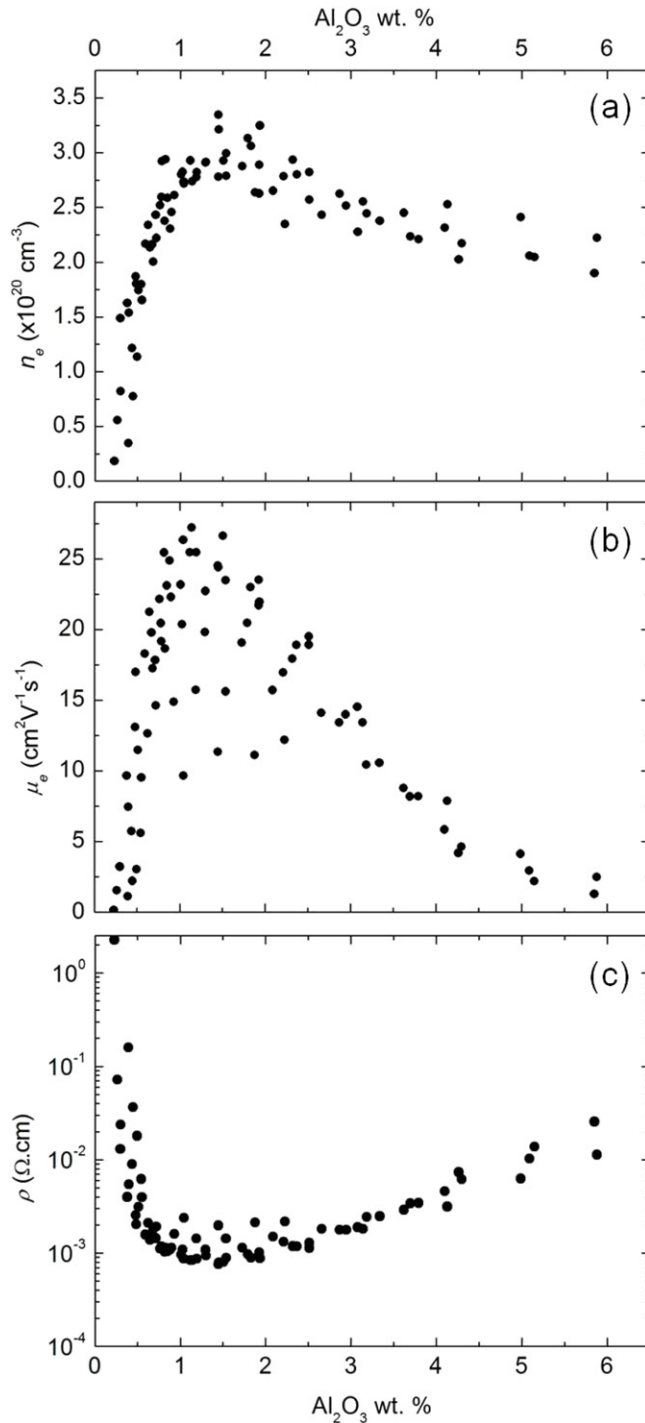


Figure 5. The distributions of (a) carrier concentration, n_e ($\times 10^{20} \text{ cm}^{-3}$), (b) carrier mobility, μ_e ($\text{cm}^2 \text{ V}^{-1} \text{ s}^{-1}$) and (c) resistivity, ρ ($\Omega \text{ cm}$) as a function of wt%. Al_2O_3 .

for the plasma frequency ω_p and the scattering parameter γ_0 from which the carrier density n_e and mobility μ_e are calculated to within 5% of values determined by van der Pauw and Hall measurements. The model may be used in conjunction with mapping spectrophotometry to accurately map the carrier concentration across co-sputtered samples that possess a uniform composition gradient. However, the corresponding mapping of mobility is unreliable for lower plasma frequencies (corresponding to $n_e < 10^{20} \text{ cm}^{-3}$) and

so additional mapping of the sheet resistance, e.g. via 4-point probe measurements, is required. Further investigations into the low frequency scattering of charge carriers in doped ZnO films, via ac measurements, are necessary to determine a more accurate expression for $\gamma(\omega)$ than that currently used within the model (equation (5)). It is hoped that this will lead to an improvement in the model's ability to extract mobility values directly from transmittance data and thus eliminate the need for secondary electrical measurements.

This combinatorial approach towards the electrical optimization of TCO materials holds great advantages: firstly, the need to process large sample sets, within which the composition of each sample is varied incrementally, is eliminated. The deposition of a single co-sputtered sample, plus the determination of the growth profiles from each individual target, is sufficient to effectively probe the relationship between composition and opto-electronic properties. The speed with which new doping routes can be investigated is therefore significantly higher. Secondly, the relationship between composition and subsequent film properties can be determined with a much higher resolution than with an incremental sample set. The resolution may be improved further simply by increasing the number of scan points over the sample. Thirdly, the effects of any run to run variation in the deposition parameters over a large sample set are removed through the use of a single combinatorial sample. A higher degree of confidence can therefore be placed in the result of the subsequent analysis.

It is important to note that the optical model can be used to fit optical spectra measured via scanning ellipsometry. However, the maximum range of the ellipsometer used within this investigation was limited to 1600 nm compared with 2700 nm for spectrophotometry. The model's Drude component is therefore likely to be less successful at extracting electrical parameters from ellipsometric spectra.

To conclude, the best opto-electronic performance for RF sputtered Al doped ZnO, using the described methodology, was achieved for a composition of 1.5 wt%. Al_2O_3 and corresponded to a resistivity of $7.6 \times 10^{-4} \Omega \text{ cm}$ and an average optical transmittance of 86% (over 300–850 nm). Uniform films of AZO with these properties may be achieved simply by tuning the relative growth rates (i.e. by changing the RF power) from one or both of the target materials to achieve a 1.5 wt%. composition at the centre-point of the substrate and by rotating the substrate throughout deposition. Such films are considered good candidates for transparent contact layers in thin-film PV devices—a film thickness of $\sim 750 \text{ nm}$ giving rise to a sheet resistance of $\sim 10 \Omega/\square$. The combinatorial approach to the optimization, with respect to the requirements of thin-film PV, of sputtered Al doped ZnO films is therefore demonstrated. Future work should involve the application of the above methodology to investigate further doping routes to ZnO and the incorporation of optimized doped ZnO films into PV devices.

Acknowledgments

This work was funded by EPSRC SUPERGEN (PV-21), grant number EP/F029624.

References

- [1] Castellano R 2010 *Solar Panel Processing* (Philadelphia, PA: Archives Contemporaines)
- [2] Bengali S, Borello D, Sauvain-Vallat E, Meir J, Kroll U and Hotzel J 2009 *Proc. 24th European PVSEC (Hamburg)* pp 21–5
- [3] Repins I, Contreras M, Egaas B, DeHart C, Scharf J, Perkins C, To B and Noufi R 2008 *Prog. Photovolt. Res. Appl.* **16** 235–9
- [4] Katagiri H, Jimbo K, Maw W, Oishi K, Yamazaki M, Araki H and Takeuchi A 2009 *Thin Solid Films* **517** 2455–60
- [5] Wang W, Diao X, Wang Z, Yang M, Wang T and Wu Z 2005 *Thin Solid Films* **491** 54–60
- [6] Igasaki Y and Saiton H 1991 *J. Appl. Phys.* **70** 3613–9
- [7] Perrenoud J, Kranz L, Buecheler S, Pianezzi F and Tiwari A 2011 *Thin Solid Films* **519** 7444–8
- [8] Drude P 1900 *Ann. Phys.* **306** 566–613
- [9] Ruske F, Pflug A, Sittinger V, Szyszka B, Greiner D and Rech B 2009 *Thin Solid Films* **518** 1289–93
- [10] Brehme S, Fenske F, Fuhs W, Nebauer E, Poschenrieder M, Selle B and Sieber I 1999 *Thin Solid Films* **342** 167–73
- [11] Blatt F J 1957 *J. Phys. Chem. Solids.* **1** 262–9
- [12] Brooks H 1951 *Phys. Rev.* **83** 879
- [13] Chattopadhyay D and Queisser H 1981 *Rev. Mod. Phys.* **53** 745–68
- [14] Wooten F 1972 *Optical Properties of Solids* (New York: Academic)
- [15] Fox M 2010 *Optical Properties of Solids* (Oxford: Oxford University Press)
- [16] Treharne R E and Durose K 2011 *Thin Solid Films* **520** 1313–7
- [17] Smith R A 1961 *Wave Mechanics of Crystalline Solids* (London: Chapman and Hall)
- [18] Burstein E 1954 *Phys. Rev.* **93** 632–3
- [19] Moss T S 1954 *Proc. Phys. Soc. B* **67** 775–82
- [20] Schmidt H M and Weller H 1986 *Chem. Phys. Lett.* **129** 615–8
- [21] Krishna M and Friesner R 1991 *J. Chem. Phys.* **95** 8309–22
- [22] Urbach R 1953 *Phys. Rev.* **92** 1324–5
- [23] Kramers H A 1927 *Trans. Vol. Cen. Cong.* **2** 545–7
- [24] Kronig R 1926 *J. Opt. Soc. Am.* **12** 547–56
- [25] Woollam J A Co., Inc. 2009 *CompleteEASE™ Data Analysis Manual* (Lincoln, NE: J A Woollam Inc.)
- [26] Synowicki R A 2008 *Phys. Status Solidi c* **5** 1085–8
- [27] Synowicki R A, Johs B D and Martin A C 2011 *Thin Solid Films* **519** 2907–13
- [28] Theiss M 2012 *Scout 3.0, Hard and Software for Optical Spectroscopy* (Aachen, Germany)
- [29] Macleod H A 1986 *Thin-Film Optical Filters* (Bristol: Hilger)
- [30] Nelder J and Mead R 1965 *Comput. J.* **7** 308–13
- [31] Minami T, Sato H, Ohashi K, Tomofuji T and Takata S 1992 *J. Cryst. Growth* **117** 370–4
- [32] Pisarkiewicz T and Kolodziej A 1990 *Phys. Status Solidi b* **158** K5–K8
- [33] Ellmer K 2001 *J. Phys. D: Appl. Phys.* **34** 3097–108
- [34] Kane E 1957 *J. Phys. Chem. Solids* **1** 249–61
- [35] Faÿ S, Steinhauser J, Oliveira N, Vallat-Sauvain E and Ballif C 2007 *Thin Solid Films* **515** 8558–61